OBSERVATION OF A CURVATURE DRIVEN, TRAPPED PARTICLE MODE CREATED BY A POTENTIAL BARRIER

by

J. C. Fernandez, C. P. Chang, A. J. Lichtenberg
M. A. Lieberman and H. Meuth

Memorandum No. UCB/ERL M85/41
24 May 1985

ELECTRONICS RESEARCH LABORATORY

College of Engineering
University of California, Berkeley
94720

Observation of a Curvature Driven, Trapped Particle Mode Created by a Potential Barrier

J. C. Fernandez, C. P. Chang, A. J. Lichtenberg, M. A. Lieberman
and H. Meuth

Department of Electrical Engineering and Computer Sciences
and the Electronics Research Laboratory
University of California, Berkeley, CA 94720

ABSTRACT

A mirror-confined hot-electron distribution is created using high-power short-pulse ECRH, in a single, good curvature (magnetically stable) cell of a plasma-filled multiple mirror device. The hot electrons are observed to decouple good and bad curvature regions on the two sides of the hot electron cell. An unstable MHD-like, rigid plasma motion to the walls occurs in the bad curvature region, with velocity comparable to that of a mode driven by the bad curvature alone. In some magnetic configurations the plasma restabilizes later in time. The hot-electron distribution decays stably, independent of the other processes. The initiation of the instability is correlated with the appearance in the hot-electron cell of a negative potential barrier. For the configurations in which plasma is restabilized, the restabilization is correlated with the decay of the potential barrier due to ion trapping in the hot electron cell. An electron beam time-of-flight probe has been used to measure the potential barrier and its decay. The experimental results are compared to a curvature driven, trapped particle theory, including the effects of finite collisionality.

I. Introduction

One of the most promising configurations being investigated for confinement of fusion plasmas is that of a tandem mirror in which a potential barrier to electron flow is formed between regions of unstable and stable magnetic curvature.[1] In the absence of the barrier the entire pressure weighted curvature is stable. This configuration has been analyzed in the collisionless limit, using drift-kinetic equations, to study trapped particle modes.[2] The result is that the plasma is unstable if the ratio of passing-to-total electron density in the unstable region is sufficiently small, an approximate stability criterion being (for the lowest order m = 1 azimuthal mode)

$$\frac{n_t}{n_0} > 4\,\frac{r_p}{R}$$

where n_t/n_0 is the ratio of the "sheath" or passing density (which samples both the stable and unstable curvature regions) to the unstable plasma density, and r_p/R is the ratio of plasma radius to the average unfavorable radius of curvature in the unstable region. The preceding equation implies that the usual tandem mirror configuration would be unstable for a fully developed plasma sheath, in which $n_t/n_0 \approx (m_e/m_i)^{1/2}$ to preserve the Boltzmann distribution of electrons [$(m_e/m_i)^{1/2} \approx 1/40$, for hydrogen]. Theoretically, it should be possible to tailor the machine design such that the potential barrier serves its confinement function without producing this trapped particle instability.[3]

A resistive trapped particle instability is also expected to be present in tokamaks, where the prediction is that high mode numbers are unstable, leading to plasma turbulence.[4] Although turbulence is commonly seen in tokamaks, under conditions in which the trapped particle mode should exist, positive identification has not been possible. The dissipative trapped electron mode has been observed[5] in a linear magnetic field configuration. The trapping was achieved by the mirror throats of the single mirror cell in the device, with about 60% of the electron population trapped in the mirror cell, large enough to observe the density gradient driven electron dissipative mode. Typical of density gradient driven modes, the mode was radially localized in the region of maximum density gradient and saturated without gross plasma loss with a saturation level for density fluctuations of about 30%.

Unlike the above experiments, in the tandem mirror configuration a mode can be driven by unfavorable curvature, in which the most dangerous perturbation is an m = 1 azimuthal variation that is not radially localized, having transverse plasma flow to the walls. The mode is expected to be strongly localized in the unstable cell and thus be similar to modes observed in early experiments in which a mirror-confined plasma with MHD unstable curvature was terminated, outside of the mirrors, on a non-emitting surface.[6,7,8,9]

It is the purpose of the present paper to describe experimental observations of instabilities in tandem-mirror-like magnetic configurations having a negative potential separating stable and unstable curvature regions, in which MHD modes localized in unstable curvature regions are produced. The results are compared with a theory of trapped particle instabilities in a regime for which the curvature drive dominates the instability mechanism, but where collisional effects are also important.

II. Experimental Configuration

The measurements are performed in the magnetic mirror system (MMX) shown in Fig. 1. The magnetic field is pulsed, with a rise time of 200 μsec and a decay time of 2 msec. Plasma injected from a Marshall gun source flows along a 225 cm region with a 0.18 T axial magnetic field and through a quadrupole stabilized mirror field or a cusp field at T_8, then into three or more cells with midplanes at M_{78}, M_{67}, and M_{56}, etc. Each cell has length l = 75 cm and midplane field $B_0 =$ 0.18 T. The cell at M_{67} has stable mirror-quadruple fields having mirror ratio R = 3.0 and fan ellipticity $Q \approx 20$. The cells with midplanes at M_{56} and beyond may be stabilized, partially destabilized or fully destabilized, depending on the particular magnetic configuration for the experiment.

The 10 cm diameter metal chamber wall of the central cell M_{67}, together with mesh-covered endplates at T_6 and T_7 having openings shaped to fit the elliptical flux surfaces, form a cavity for electron cyclotron resonance heating (ECRH) that does not obstruct the plasma flow. A 3 μsec, 250 kW, 9.0 GHz, rf heating pulse is injected into the plasma-filled cavity at M_{67}. This creates a magnetically confined, hot electron density n_h in the center cell due to ECRH at the two resonance zones, each approximately 6 cm from the mirror throats.

Diagnostics to measure the various plasma parameters include the following: The plasma density in the ECRH cell is measured using an 8 mm, swept-frequency microwave interferometer of conventional design.[10,11] The interferometer has been calibrated against a commercial phase shifter using rods and slabs of various dielectric constant and radii inserted into the ECRH cavity. The frequency is swept every six microseconds, yielding reliable measurements for plasma densities in the range $10^{11}-10^{13}$ cm^{-3} on 6 μsec timescales.

The temperature T_h of the "tail" of the hot electron distribution is determined from the measured x-ray flux in the 1-10 keV range using a cooled, Si(Li) detector with a beryllium window having 47 and 91 percent transmissivity at 1 keV and 2 keV, respectively. The energy resolution of the system is typically 0.4 keV, and the maximum count rate is 500 kHz. Although there is some line radiation observed from high-Z plasma impurities, those with significant amplitudes are sufficiently separated to leave a useful, line-free window between 1.5 and 4 keV to observe the plasma x-ray bremsstrahlung radiation. The preceding measurements are corroborated with a diamagnetic loop which determines the density-energy product of the ECRH plasma just after its formation. The loop and its associated electronics have been calibrated by placing a small solenoid inside the ECRH cell and driving the solenoid current with a square wave generator.

It is necessary to determine the radial plasma profile in order to analyze the interferometer and diamagnetic loop measurements. Arrays of four cylindrical Largmuir probes biased into ion saturation were used to obtain time-resolved radial profile measurements in the central cell midplane in the absence of ECRH, and in the two adjacent cell midplanes with and without ECRH. (Profile measurements in the central cell midplane in the presence of ECRH could not be performed due to arcing at the probe tips). We observed little change in radial profile in the adjacent cells with and without ECRH, and little change in the profiles as a function of time.

For some plasma source and vacuum conditions, the plasma density in the central cell rises sharply just after ECRH. A nude ion gauge is used to monitor the transient pressure rise in the central cell produced by the emission of neutrals from the plasma source and the chamber walls. We interpret some fraction of the plasma density rise after ECRH as being due to ionization of this transient neutral pressure rise, with the remaining density rise resulting from the potential barrier dynamics, as described subsequently.

To measure the potential barrier in the central cell, an electron beam time-of-flight diagnostic has been developed.[12,13] A schematic of the diagnostic arrangement is shown in Fig. 2. The electron beam is injected in the midplane of a cell adjacent to the ECRH cell, traverses that cell, and is detected in the midplane of the following cell. To determine the beam time-of-flight, the beam current is modulated at f = 10 MHz, and the phase delay of the signal received at the collector is measured. To provide high signal-to-noise ratio, a digital, phase-locked loop is used.

The phase $\varphi(x)$ due to an axial potential distribution $V(x)$, with respect to the beam cathode at x = 0, is given by

$$\varphi(x) = \omega t(x) = \omega \int_0^x \frac{dx}{v(x)} \ , \tag{1}$$

where

$$v(x) = \left[\frac{2e\ V(x)}{m}\right]^{1/2} \ ,$$

is the beam velocity. If we assume a simple square well model for the potential, then the phase change $\Delta\varphi$ at $x = 2l$ due to the creation of a negative barrier of magnitude Φ and length l is

$$\Delta\varphi = \frac{\omega l}{v}\left[\left(1 - \frac{\Phi}{V}\right)^{-\frac{1}{2}} - 1\right] \tag{2}$$

Equation (1) has been verified experimentally by applying a -45 V, 100 μsec pulse to a 2.5 cm diameter ring electrode placed on axis at the midplane of the center cell. The dependence of $\Delta\varphi$ on V in (2) has also been verified over the range from 100 to 200 volts. The time response of the beam diagnostic has been measured by applying a 20 V, peak-to-peak, 25 kHz square wave modulation in series with the cathode voltage. These measurements yield a response time that is less than 5 μsec. The electron beam diagnostic has been used to observe the formation and decay of -40 to -60 volt barriers on 10 microsecond timescales.

The transient plasma density and plasma motion in the adjacent cells are measured using Langmuir probe arrays in the cell midplanes, as described previously. the probes are biased into ion saturation, and the Laframboise theory[14] is used to infer the density from the observed ion current. The transient plasma potentials in the adjacent cell midplanes are measured using high impedance, emissive probes. These same probes, either non emitting or at low emission currents, are used to measure the floating potentials.

Transient measurements of the cold plasma temperature are required to relate the barrier potential to the temperature, and are also useful for determining the collisionality regime and the theoretical growth rate of the trapped particle instability. To use Langmuir probes as a fast electron temperature diagnostic, the probe bias voltage is swept sinusoidally, with every bias cycle producing an I vs. V plot, ranging from the ion saturation to the electron saturation region. On each plot, the exponential region yields the electron temperature from the relation

$$\ln(I-I_i) = \ln I_e + \frac{V-V_P}{T_c}$$

where I_i and I_e are the ion and electron saturation currents, respectively, and V_P is the plasma potential. A typical sweep frequency of 250 kHz gives a time resolution of 4 μsec. The main complication to the bias sweeping is the finite capacitance from the probe tip to the chamber ground. Thus, in addition to plasma currents, the bias transformer drives a capacitive current through the current load resistor. This capacitance is tuned out by a bridge circuit , but only at a single plasma density. The result is a hysteresis in the $I-V$ plot which can be mostly eliminated by computer processing.

Typical transient temperature characteristics in cell midplanes M_{56} and M_{78} are shown in Figs. 3a and 3b. The error bars are due to hysteresis in the $I-V$ swept voltage measurements. The temperature at M_{56}, which is the important cell for determining the characteristics of the mode, jumps from somewhat below 10 eV to, perhaps, 15 eV immediately after ECRH. There follows a fall back to about 10 eV and then an apparent rise, which is both unexplained and uncertain. However this later period is not important for the calculations. The rise immediately after ECRH is thought to be due to r.f. leakage into the adjacent cells.

Typical plasma parameters at the initiation of the ECRH pulse are $T_c = T_i \approx 7\text{-}8$ eV and $n_{67} \approx 3\times10^{11}\text{cm}{-3}$, with the density decreasing by about a factor of 1.5-2.0 from cell to cell away from the source. After ECRH, the exponential tail of the hot electron distribution, obtained from pulse height analysis of x-rays, indicates $T_h \approx$ 1.5 keV. The average energy of the hot electrons, obtained from the diamagnetic loop and microwave interferometer, together with measurements of the radial density profile in adjacent cells, is generally about a factor of two lower, indicating a non-Maxwellian distribution of the hot electrons. As we will subsequently show from potential measurements in the ECRH cell, most electrons in that cell are heated sufficiently to be magnetically trapped.

The sudden appearance of the hot-electron population, and the corresponding sudden reduction of the cold-electron population initiates formation of a negative potential barrier near throats T_6 and T_7 as follows: The potential V_7 of midplane M_{67} with respect to midplane M_{78} is related to the cold (non-magnetically confined) electron densities n_{67} and n_{78} by the Boltzmann relation. If $n_{67} < n_{78}$, a negative potential barrier forms near T_7

$$V_7 = -T_c \ln(n_{78}/ n_{67}) \quad , \qquad (3)$$

where T_c is the cold-electron temperature. A similar expression determines V_6. These expressions are invalid in the limit $n_{67} \to 0$, where the ion flow dynamics must be considered. For this case, the potentials can be estimated by equating the total ion flux to the total electron flux entering the center cell. Using, for example, a Bohm velocity for the ions, we have (for V_6, $V_7 < 0$)

$$(n_{56}+n_{78})(T_c/\varepsilon m_i)^{1/2} = [n_{56}\exp(V_6/T_c) + n_{78}\exp(V_7/T_c)](8T_c/\pi m_e)^{1/2} \tag{4}$$

where m_i and m_e are the ion and electron masses and ε is the natural base. When the Boltzmann relation is valid for the densities and potentials between M_{56} and M_{78} we obtain, using (3)

$$V_7 = T_c\left[\ln\left(1 + \frac{n_{56}}{n_{78}}\right) - \frac{1}{2} - \frac{1}{2}\ln\left(\frac{2m_i}{\pi m_e}\right)\right] . \tag{5}$$

A similar expresion holds for V_6. For hydrogen ions with $n_{56} = n_{78}$, we find

$$V_7 = V_6 \approx -3.8\,T_c \tag{6}$$

which serves as an estimate of the initial potential.

The potential barrier is destroyed on the timescale for ions to enter into and become trapped in the center cell. By quasi-neutrality, cold electrons accompany the trapped ions, and therefore n_{67} increases on the ion trapping timescale. The final state in this idealized model ($n_{56} = n_h = n_{78}$ = const, initially, T_c = const) is n_{67} (cold) $\approx n_h$ and $V_6 = V_7 \approx 0$. The total electron density (hot + cold) rises to twice its initial value after the barrier destruction. Non-ideal effects important in the experiment include: initial axial density variations, ion dynamics including non-zero transit times, heating of cold electrons by hot electrons, ionization of background gas, and plasma loss processes. These effects have been taken into account in more complete model[12,13] and only the results of the calculation are presented here for comparison with the experiment.

In Fig. 4a, the experimentally measured phase delay (2) for the electron beam probe is given, with error bars due to noise indicated. Only the change in phase shift after ECRH (t=0) is significant. The corresponding values Φ/T_c, obtained from the phase shift measurement by assuming a temperature $T_c = 15eV$, are given in Fig. 4b. The change in the density at M_{67}, as measured by the interferometer, is given in Fig. 4c.

These results are compared with the model in Fig. 5. In Fig. 5a, the phase delay evolution predicted by the initial plasma conditions is given, corresponding to the predicted potential evolution in Fig. 5b. The predicted density variation in the cell is given in Fig. 5c. The model is seen to give a potential similar to the experimental results except that the decay of the potential barrier occurs somewhat earlier. This may be due to an underestimation of the effect of cold electron trapping due to heating of the cold electrons by the hot. The slower decay of the model density in the ERHC cell also indicates the need for some refinements. However, experimentally, the existence of a potential barrier of between 3 and 4 T_c is clearly established and will be used in comparing the experimental results of the trapped particle mode to theoretical predictions.

III. Observations of the Instability

The experimental observations of the trapped particle mode come from arrays of Langmuir probes biased into ion saturation. With an array of probes placed on a cross sectional plane of the machine, and a suitable radial density profile model, continuous temporal information, like the plasma centroid's position and density, can be obtained. Observations with three and four probe arrays have been used. The radial density profile has been measured to conform approximately to a Gaussian density profile,

$$n(x,y) = n_0 \exp\left[\frac{-[(x-x_0)^2 + (y-y_0)^2]}{2r_p^2}\right] \tag{7}$$

where n_0 is the peak density, (x_0,y_0) is the centroid position, and r_P is the plasma radius. With an array of four probes in suitable positions in the (x,y)

plane, and with the assumption of a circularly symmetric radial profile ($m = 0,1$ modes only), the four variables $x_0(t)$, $y_0(t)$, $n_0(t)$, $r_P(t)$ can be determined as a function of time. With an array of three probes, and assuming a constant r_P (no $m = 0$ mode), the other three variables can be determined. If the dominant azimuthal mode is higher than $m = 1$, the data yields either no solution or rapidly fluctuating solutions for the plasma centroid position and peak density, in which case the data is discarded.

Three magnetic field configurations were employed in the studies of trapped particle modes. In the first, shown in Fig. 1, the plasma is injected from the Marshall gun through a solenoidal section into a rising axisymmetric double cusp at T_8. The downstream magnetic configuration consists of the solenoidal field throughout the device, two fan shaped quadrupole mirror throats at T_7, and T_6, and simple axisymmetric mirror throats from T_5 to T_0 (the bad curvature region where the trapped particle mode amplitude will be high). With proper plasma source settings the double cusp in T_8 is filled with plasma and its strong stable curvature can provide MHD stability for the system as a whole. The density falls by a small factor (less than 2) from cell to cell, but is reasonably constant within each cell. The entire system tends to be only weakly stable, and becomes flute unstable late in time as the double cusp empties. Because of the instability late in time, restabilization of the trapped particle mode was generally not observed as the potential barrier decayed.

In the second configuration, the currrent in the T_5 mirror throat is reversed, to create an axisymmetric double cusp there as in T_8. This configuration would be expected to be more stable than the previous one, and possibly completely stable, depending on the axial density distribution. Mirror cell M_{56} was found to be unstable at the time of creation of the potential barrier, but generally the plasma restabilized after the potential barrier decayed.

Measurements of the axial density distribution at M_{56} and in the neighborhood of the double cusp at T_5 are shown in Fig. 6, and indicate a density distribution which was lower near the double cusp than at the midplane at the time of initiation of the ECRH. The pressure-weighted curvature is calculated to be unstable for cell M_{56}, alone, and to be stable for the system of three cells (M_{56}, M_{67}, M_{78}).

In the third configuration, the device was run with quadrupole-stabilized fields in all cells, producing good curvature drive in all cells. This configuration was found to be stable to trapped particle modes.

Figure 7 shows the ion densities obtained using two Langmuir probes on axis, one at M_{78} and the other at M_{56} for the first configuration. At time $t = 0$, the ECRH pulse heats the plasma electrons in M_{67}, which remain mirror confined for a relatively long time. Evidence for the presence of hot electrons comes from their steady bremsstrahlung x-ray emission. The Langmuir probe signal at M_{78}, decreasing exponentially after the Marshall gun injection, shows a sharp rise after ECRH. After subtracting an electrical noise spike, there is an increased signal, interpreted as a combination of a density increase and a temperature increase from ECRH field leakage from M_{67}. This additional plasma decays rapidly, in about 50 μsec, with the temperature decay even more rapid. The plasma in cell M_{78} remains stable after ECRH. In M_{56}, the plasma dumps in a few microseconds, evidencing a strong axially localized instability. We interpret this as a decoupling of the plasma in cells M_{01}--M_{56} from the plasma in cells M_{67}--M_{78}, such that the former cells are unstable while the latter cells remain stable. The plasma motion in M_{56} was confirmed for a shot taken under similar conditions, as mapped by a four-probe array, indicating a time of the order of 5 μsec to move a distance of the order of the plasma radius.

Most probe-array measurements were obtained in the second configuration with a double cusp at T_5. Figure 8 gives a typical shot showing the plasma centroid position (dots) at various times, indicating at M_{56} a rapid motion to the chamber wall, an apparent bounce off the wall with some plasma loss, followed by a somewhat slower movement back toward the wall. Later in time the plasma restabilizes at the center. Throughout the unstable motion in M_{56}, the plasma in M_{78} remains well centered, indicating a stable plasma. For this shot with good ECRH heating, the tail of the x-ray distribution, assumed Maxwellian, indicated a temperature of $T_h \approx$ 1.5 keV, and the diamagnetic loop signal indicated an average hot-electron energy of $E_h \approx$ 420 eV. This is similar to the hot electron distribution in the case in which the phase shift, measured by the electron beam time-of-flight apparatus, indicates that a deep potential well exists which decouples M_{56} and M_{78} during the unstable time, but decays away at about the time that the plasma restabilizes in M_{56}.

The data for another shot, is presented in Fig. 9. Here the diamagnetic loop signal and the plasma density measurements yield an average hot electron energy of $E_h \approx$ 280 eV. This relatively low temperature is corroborated by the weaker, faster decaying x-ray signal, and by the decrease in plasma creation due to neutral gas ionization in the adjacent cell M_{78}. The collision frequency for these hot electrons is much higher than that of the hot electrons in the shot shown in Fig. 8, so we expect the barrier to decay much faster. We see in Fig. 9 that the restabilization occurs earlier, plasma motion having essentially been reduced to a small value at a time between 15 and 20 μsec after ECRH. This is in contrast to the shot shown in Fig. 8 in which there is still considerable motion at 50 μsec after ECRH. A number of phase shift measurements were made on ECRH plasmas in configuration 2, with plasma conditions as in Fig. 9. A typical phase shift measurement from such a shot is shown in Fig. 10. Here we see, after the initial establishment of the barrier, a rather rapid decay of the phase shift. The more rapid restabilization of the mode seen in Fig. 9 would be the expected consequence of this rapid decay.

For the magnetic field configuration (3) in which fully stabilized quadrupole fields are employed, the plasma centroid remained centered at both M_{56} and M_{78} throughout the establishment and decay of the potential barrier. This indicates that the mode observed in configurations (1) and (2) was essentially curvature driven. If a resistive mode was also present it saturated at a low amplitude and was therefore not observable as gross motion of the plasma centroid.

IV. Comparison of Experiment with Theory

To obtain a comparison of theory with experiment, we estimate the experimental parameters required to obtain a theoretical description of the growth rate. For the collisionless case an expression for the mode frequency has been obtained, which, for low passing fraciton can be approimated by[2]

$$\omega \approx \frac{-\omega_{*i}(n_t T_c / n_0 T_i)}{2(k_\perp^2 r_i^2 + (n_t / n_0))} \pm \sqrt{-\frac{\omega_{*e}\omega_c}{k_\perp^2 r_i^2}} \qquad (8)$$

Here ω_c is the curvature drift frequency

$$\omega_c = \frac{2T_c(eV)}{-B_0 L_{eff}^2} \qquad (9)$$

where L_{eff} is the length associated with the unstable curavture drive, defined below, ω_{*e} is the electron diamagnetic drift frequency

$$\omega_{*e} = \frac{T_c(er)}{Br_p}\frac{1}{n}\frac{dn}{dr} \qquad (10)$$

r_i the ion gyroradius, n_t the density of transiting electrons, and the other symbols have their usual meanings. We define L_{eff} in terms of the quantity

$$L_{eff}^2 \equiv < 2r_p \delta r u / \delta u >_z , \tag{11}$$

where δu in the energy gain in interchanging lines at radius r_p through a distance δr. Then, in the uniform (in z) slab model, the growth rate of the instability is given by

$$\gamma_0 = v_i / L_{eff} , \tag{12}$$

where v_i is the theremal velocity of the ions at temperature $T_i + T_c$. The quantities in (11) and (12) are obtained from an MHD ballooning code,[15,16] using the actual magnetic fields and measured axial density profiles for each of the three magnetic configurations. The code solves the $m = 1$ (rigid) ballooning eigenvalue problem in the long thin approximation. For cell M_{56} in the first configuration (quadrupole at T_c and T_5 simple mirror) and taking the density to be axially uniform in each mirror cell of the many cell system (multiple mirror approximation), we obtain for a temperature of 10 eV, $\gamma_0^{-1} = 10\ \mu$sec ($L_{eff} = 53$ cm). (The downstream cell with simple mirrors at lower densities have very similar values of L_{eff}). For the second configuration (with a double cusp at T_5), the growth rate depends sensitively on the axial density distribution. This was measured at the accessible points with the results shown in Fig. 6. The decrease in the density from the unstable curvature region near the mirror throat at T_6 to the region of the stable curvature cusp at T_5 , indicates that the configuration may be unstable. Calculations were made using various axial distributions decreasing from the mirror throat T_6 to the double cusp at T_5 but within the range of experimentalobservations given in Fig. 6. They indicated that the growth rate could be of the same order as for the simple mirrors, or the distribution could be more stable.

Using the measured experimental values of the various parameters and the calculated value of L_{eff}, we obtain the values given in Table 1. The parameter ranges account for both shot-to-shot variability and measurement uncertainty.

Substituting these values in Eq. (8), with $\omega = \omega_r \pm i\gamma$ we obtain

$$5\times10^4 < \gamma < 1.5\times10^5 \mathrm{sec}^{-1}$$

$$10^4 < \omega_r < 5.7\times10^4 \mathrm{sec}^{-1}$$

We note that the highest value of the growth rate corresponds to the highest values of cold electron temperature. We can now examine the validity of various theoretical approximations. Firstly, we note that bounce averaging is permissible, since

$$|\omega|/\omega_b \approx 1.2\times10^{-2}$$

Secondly, we have

$$1.2\times10^{-3} < |\omega|/\nu_c < 0.65,$$

Here, the highest ratio corresponds to the highest value of cold electron temperature and to the lowest value of density. These inequalities show that although the bounce-averaged drift kinetic formalism is appropriate to describe the electron trapped particle mode in our system, we are in a collisional regime. However, the approximate agreement of our experimental characteristic loss time of 5 μs with the lower end of the collisionless growth time γ^{-1} suggests that collisions do not profoundly alter the physics of the trapped particle mode. Nevertheless, a model appropriate to our intermediate collisionality regime should be employed.

We construct a slab model in which two cells with uniform curvature drive are connected by a passing electron population through a localized potential barrier. Normally, one cell has stable curvature and the second cell has unstable curvature, with the ratio of stable to unstable curvature of the order of two, characteristic of the experiment. We assume equilibrium Maxwellian distributions in the two cells and solve the drift kinetic equation[17] at arbitrary collisionality using a Krook collision operator that conserves particles, but does not conserve momentum or energy. We bounce-average for all species and neglect any velocity dependence in ω_c and ω_*. We assume ions have only a local response, which is equivalent to making all ions trapped (this means that a mode frequency below the ion bounce frequency, corresponding roughly to an order of magnitude below ω_{*e}, would be invalid). Finally, the finite Larmor radius stabilizing terms are identified and removed, in order to describe the $m = 1$ mode. Initial results obtained using this collisional model have been presented[18] and a paper describing the calculation is in preparation.

The model has been solved numerically for a representative case, corresponding to an electron temperature of 10 eV. The density is taken to be $2 \times 10^{11}\mathrm{cm}^{-3}$ in the unstable curvature cell and $5 \times 10^{11}\mathrm{cm}^{-3}$ in the stable cell. The curvature drift frequency in the unstable cell is taken to be 530 Hz. All other parameters are given in Table 1, with the peak potential barrier taken to be $4T_c$, corresponding to a 0.006 electron passing fraction. Before the barrier is established, equilibrium along a field line fixes the initial electron passing fraction at 0.31 in the unstable cell.

To compare the theory with experiment we use a simple argument to relate the observed plasma loss time τ to the linear growth rate γ. We assume that for the $m = 1$ mode the plasma will polarize until the E × B velocity equals the velocity that the plasma would attain if subject to the radial force of the unstable magnetic well. Thus the transverse velocity v_r is obtained by equating the plasma kinetic and potential energy

$$\frac{1}{2} M v_r^2 = - \int_0^r F \cdot dr \tag{13}$$

where

$$F \approx -\frac{1}{2}\frac{Mv_i^2 r}{L_{eff}^2} ,$$

with v_i the thermal velocity of the ions at a temperature $T = T_c + T_i$. Solving for v_r we obtain

$$v_r = \frac{v_i r}{L_{eff}} . \tag{14}$$

The time to move a distance $r = r^P$ is then

$$\tau \approx 1/\gamma \tag{15}$$

which we use in the comparison of theory with experiment.

Figure 11 shows the results of the two cell model as a function of electron passing fraction, for a collisionless system (dashed lines) and for the collisionality regime in the experiment (solid lines). In Fig. 11a the growth rate γ is given, and the experimental growth rate estimated from (15) is given by error bars which indicate both the experimental variation and the factor of two uncertainty implicit in the use of (13). We conclude that the predictions of the growth rate from the theoretical model of the curvature driven trapped particle mode, valid for our parameter regime, although somewhat low, are reasonably consistent with the experimental observations. For the much larger passing fraction (~30%) in the absence of the ECRH induced potential barrier, the growth rate is predicted to be reduced by a factor of approximately ten. Since we do not observe unstable motion under these conditions, we conclude that the mode either saturates at a low amplitude as in [5] or is, in fact, stabilized.

In Fig. 1b, we compare the ratio of the mode amplitudes in the stable and unstable cells, as predicted from the code, with the experimental observations. Because of the natural time variations in the centroid position, experienced in all stable experiments, only a lower bound to the mode amplitude ratio is obtained experimentally. Again, we find reasonable consistency between theory and experiment. We also note that the experimental mode amplitude is sufficiently large that it does differentiate the theoretical predictions for small passing electron fraction (4 T_c barrier present) from the predictions for large (~30%) passing fraction (no barrier).

We note also that we do not observe large plasma losses to the walls in the absence of unstable curvature drive (third magnetic configuration), although we expect that a collisionally driven trapped particle mode may be present. This is consistent with the observation [5] that the collisionally driven mode is localized in the region of maximum radial density gradient and saturates at fluctuation levels $\delta n / n \lesssim 30\%$. We expect enhanced diffusion from this mode but no sudden dump of plasma to the walls.

V. Conclusions

The electrons in a single cell of a multiple mirror device are heated by a short pulse of ECRH power. These trapped hot electrons create a potential barrier of approximately $4T_c$ (cold electron temperature) in the adjacent cells, as measured from the phase shift of a time-of-flight electron beam probe. The magnitude of the potential barrier and the time history of its decay are in reasonable agreement with the results obtained from a one-dimensional model for the flow of electrons and ions along the field lines. The potential barrier is formed to keep the the cold electrons from entering the ECRH cell, according to the Boltzmann distribution law. The potential barrier decays due to ion trapping in the ECRH cell, but this decay is complicated by plasma production and heating of the cold electrons entering the cell, produced by the hot electron distribution.

If the magnetic field configuration is modified so that the pressure weighted distribution is stable on the average, but unstable on one side of the potential barrier generated by the ECRH distribution, then a curvature driven trapped electron mode, strongly unstable, has been experimentally observed, localized in regions of net unstable magnetic curvature. The growth rate of the mode is found to be comparable with the growth rate expected for a flute mode, driven by the pressure weighted unstable curvature, alone. The instability leads to rapid motion of the plasma column to the vacuum chamber wall, with significant loss of plasma density. The motion of the plasma column is correlated with the potential barrier measurement and found to decrease as the potential barrier decays (reconnection and restabilization of the plasma). If the magnetic field curvature is stable on both sides of the potential barrier then no gross plasma motion is observed. Thus, if a non-curvature-driven trapped particle mode is present, it saturates at a sufficiently low amplitude so as not to be observable.

A computer code has been developed which solves the drift-kinetic equation for arbitrrary collisionality, using a Krook collisional operator and a simplified two cell model. The results of the code for typical experimental conditions indicate that a trapped electron mode with a growth rate approximately equal to the local MHD curvature driven mode should exist when a large potential barrier is present. The effect of collisionality, which could arbitrarily be supressed in the model, is to lower the growth rate more abruptly with increasing passing fraction (decreasing barrier). The restabilization of the mode with decreasing potential barrier is qualitatively in agreement with the observation that collisions play some role, but not a dominating role, in the instability.

VI. Acknowledgement

The authors would like to thank B. Archer, N. M. P. Benjamin, and D. Price for their assistance in the development of the diagnostics; B. K. Kang for running the MHD ballooning code; and H. Ramachandran, R. H. Cohen, and A. K. Sen for their contributions to the theoretical model. The work was partially supported by the Department of Energy under DOE Contract DE-AT03-76ET53059.

VII. References

[1] D. E. Baldwin and B. G. Logan, Phys. Rev. Lett., **43**, 1318 (1979).

[2] T. M. Antonsen, D. E. Baldwin, H. L. Berk, M. N. Rosenbluth, and H. V. Wong, Soviet J. of Plasma Phys., to be published; see also M. N. Rosenbluth, "Topics in Plasma Instabilities: Trapped-Particle Modes and MHD," Int. Plasma Physics Conf., Goteborg, Sweden, June 1982.

[3] "Physics Basis for Axicell Design for the End Plugs of MFTF-B," D. E. Baldwin and B. G. Logan, Ed., Lawrence Livermore Laboratory, UCID 19359, April 1982.

[4] B. B. Kadomstev and O. P. Pogutse, Nucl. Fusion, 11, 67 (1971).

[5] S. C. Prager, T. C. Marshall and A. K. Sen, Plasma Phys., **17**, 785 (1975).

[6] F. H. Coensgen, W. F. Cummins, W. E. Nexsen, and A. E. Sherman, Phys. Fluids, **9**, 186 (1966).

[7] R. Prater, Phys. Fluids, **17**, 193 (1974).

[8] I. A. Brown, A. J. Lichtenberg, M. A. Lieberman, and N. Convers Wyeth, Phys. Fluids, **19**, 1203 (1976).

[9] F. F. Chen, Phys. Fluids, **8**, 752 (1965).

[10] G. Lisitano, Rev. Sci. Instr., **36**, 364 (1965).

[11] B. T. Archer, H. Meuth, and M. A. Lieberman, "Swept-Frequency 8 mm Microwave Interferometer for MMX," Report No. UCB/ERL M84/104, Electronics Research Laboratory, University of California, Berkeley, CA (1984).

[12] C. P. Chang, J. C. Fernandez, A. J. Lichtenberg, M. A. Lieberman, and H. Meuth, Bull. Am. Phys. Soc., **29**, 1227 (1984).

[13] M. A. Lieberman and C. P. Chang, "Electron Beam Time-of-Flight Measurements of Plasma Potential in Tandem Mirrors," Report No. UCB/ERL M84/92, Electronics Research Laboratory, University of California,

Berkeley, CA (1984).

[14] J. La Framboise, "Theory of Spherical and Cylindrical Langmuir Probes in a Collisionless Maxwellian Plasma," U. Toronto Inst. for Aerospace Studies, Report No. 100 (1966).

[15] L. D. Perlstein, T. B. Kaiser, and W.A. Newcomb, Phys. Fluids, **24** 1326 (1981).

[16] T. B. Kaiser, W. M. Nevins, and L. D. Perlstein, Phys. Fluids, **26** 351 (1983).

[17] T. M. Antonson, Jr. and B. Lane, Phys. Fluids **23** 1205 (1980).

[18] H. Ramachandran, A. Sen, R. Cohen, M. Lieberman and A. Lichtenberg, Bul. Am. Phys. Soc. **29** 1187 (1984).

Table 1. Typical Experimental Parameters

Plasma radius $r_p \approx 1$ cm;

Midplane magnetic field $B_0 \approx 1.5$ kG;

Magnetic mirror ratio R = 2.8;

Potential barrier height $\Phi_b / T_c \approx 4$;

Passing cold electron fraction $n_t / n_0 \approx 0.006$;

Ion temperature $T_i \approx 5$ eV;

Plasma density $1\times10^{11} \leq 5\times10^{11}$ cm^{-3};

Cold electron temperature $5 \leq T_c \leq 15$ eV;

Curvature drive length $L_{eff} \approx 50 cm$;

Electron diamagnetic drift frequency $3.3\times10^5 < \omega_{*e} < 1.0\times10^6$ s^{-1};

Finite gyroradius parameter $k_\perp^2 r_i^2 = r_i^2 / r_p^2 \approx 0.046$;

Ion diamagnetic drift frequency $\omega_{*i} \approx 3.3\times10^5$ s^{-1};

Cold electron bounce frequency $7.8\times10^6 < \omega_b < 1.4\times10^7$ s^{-1};

Cold electron 90° collision frequency $2.3\times10^5 < v_c < 1.2\times10^7$ s^{-1};

Average unstable curvature drift frequency $0.45\times10^3 < \omega_C < 1.3\times10^3$ s^{-1}; Ratio of stable to unstable curvature frequencies $|\omega_c / \omega_s| \approx 2$.

Figure Captions

Fig. 1 Experimental configuration 1, including a schematic (not to scale) of two magnetic field lines 180 ° apart.

Fig. 2 Electron beam diagnostic set-up.

Fig. 3 Results of swept-voltage, Langmuir probe, cold electron temperature measurements: (a) in cell M_{56}; (b) in cell M_{78}. Vertical lines are error bars.

Fig. 4 Experimental data for a representative shot with good heating ($T_h \approx 1.5keV$ from x-ray tail): (a) observed phase shift; (b) normalized potential assuming $T_c = 15eV$; (c) density in ECRH cell.

Fig. 5 Values computed from model corresponding to parameters of experimental results of Fig. 4: (a) phase shift; (b) normalized barrier potential; (c) normalized density in ECRH cell.

Fig. 6 Experimental configuration 2: observations of density in cell M_{56} used for the calculation of pressure weighted curvature drive.

Fig. 7 Typical shot for experimental configuration 1, showing density variation in stable and unstable cells.

Fig. 8 Experimental configuration 2 with strong potential barrier: plasma centroid motion in the unstable (left) and stable (right) mirror cells (a) early in time; (b) later in time. The numbers are times in μsec, with $t = 0$ corresponding to the ECRH time.

Fig. 9 Experimental configuration 2 with weak potential barrier: plasma centroid motion after ECRH (a) early in time; (b) later in time.

Fig. 10 Phase shift for poor heating, showing rapid decay of the potential barrier.

Fig. 11 Comparison of theory and experment for: (a) growth rate γ; (b) ratio R of unstable cell to stable cell mode amplitudes. The abscissa $n_t/\bar{n}$ is the ratio of the density to the mean density in the stable and unstable cells $\bar{n} = (n_s n_u)^{1/2}$, where n_s is the density in the stable cell and n_u the density in the unstable cell. $T_e = 10$ eV, $T_i = 5$ eV. The dashed line is the collisionless approximation and the solid line is with collisions included. For that case we set $n_s = 10^{12} cm^{-3}$ and $n_u = 3\times10^{11} cm^{-3}$.

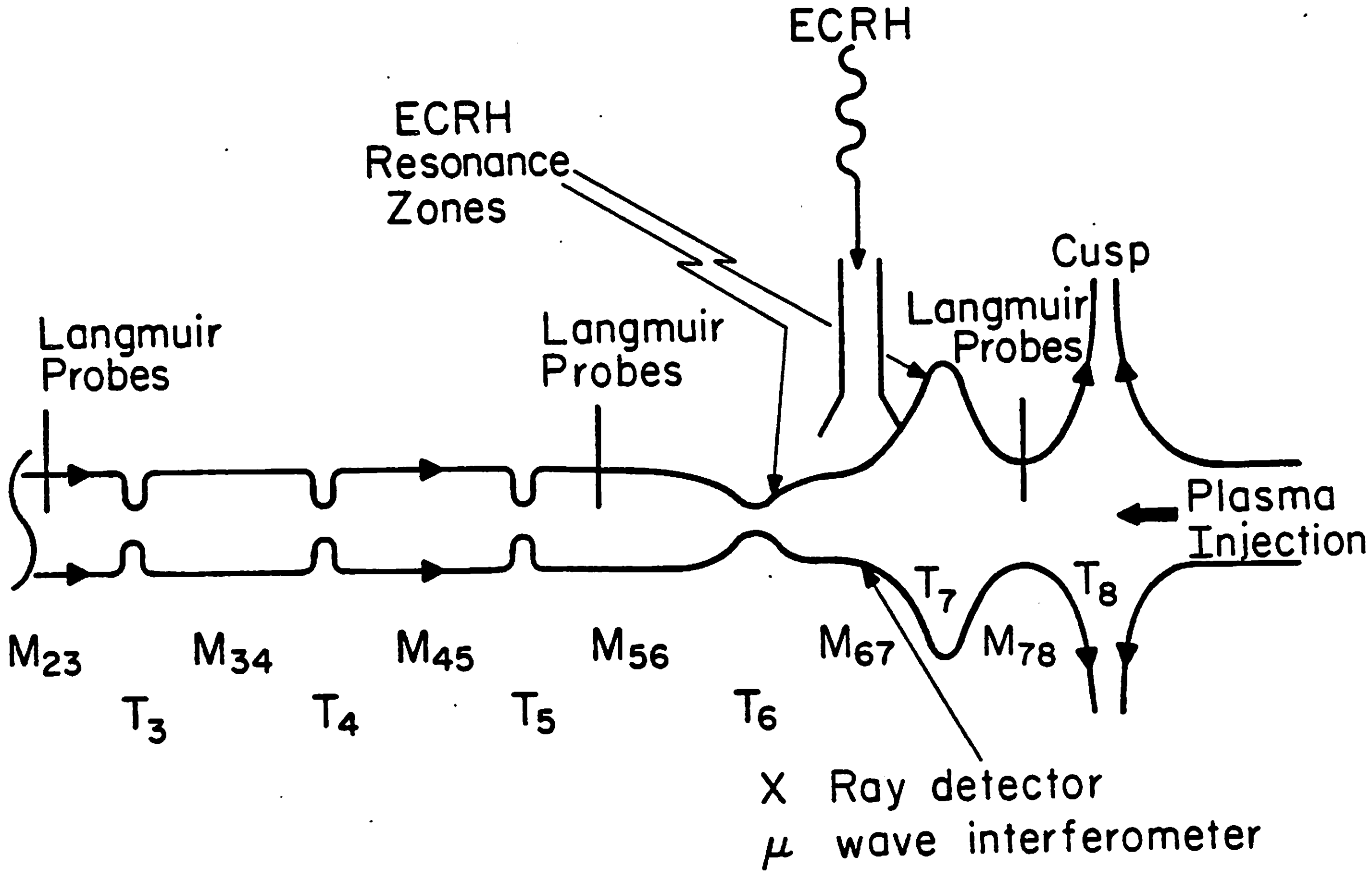
ECRH
ECRH
Resonance
Zones
Cusp
Langmuir
Probes
Langmuir
Probes
Langmuir
Probes
Plasma
Injection
M23
M34
M45
M56
M67
M78
T3
T4
T5
T6
T7
T8
X Ray detector
μ wave interferometer

Fig. 1

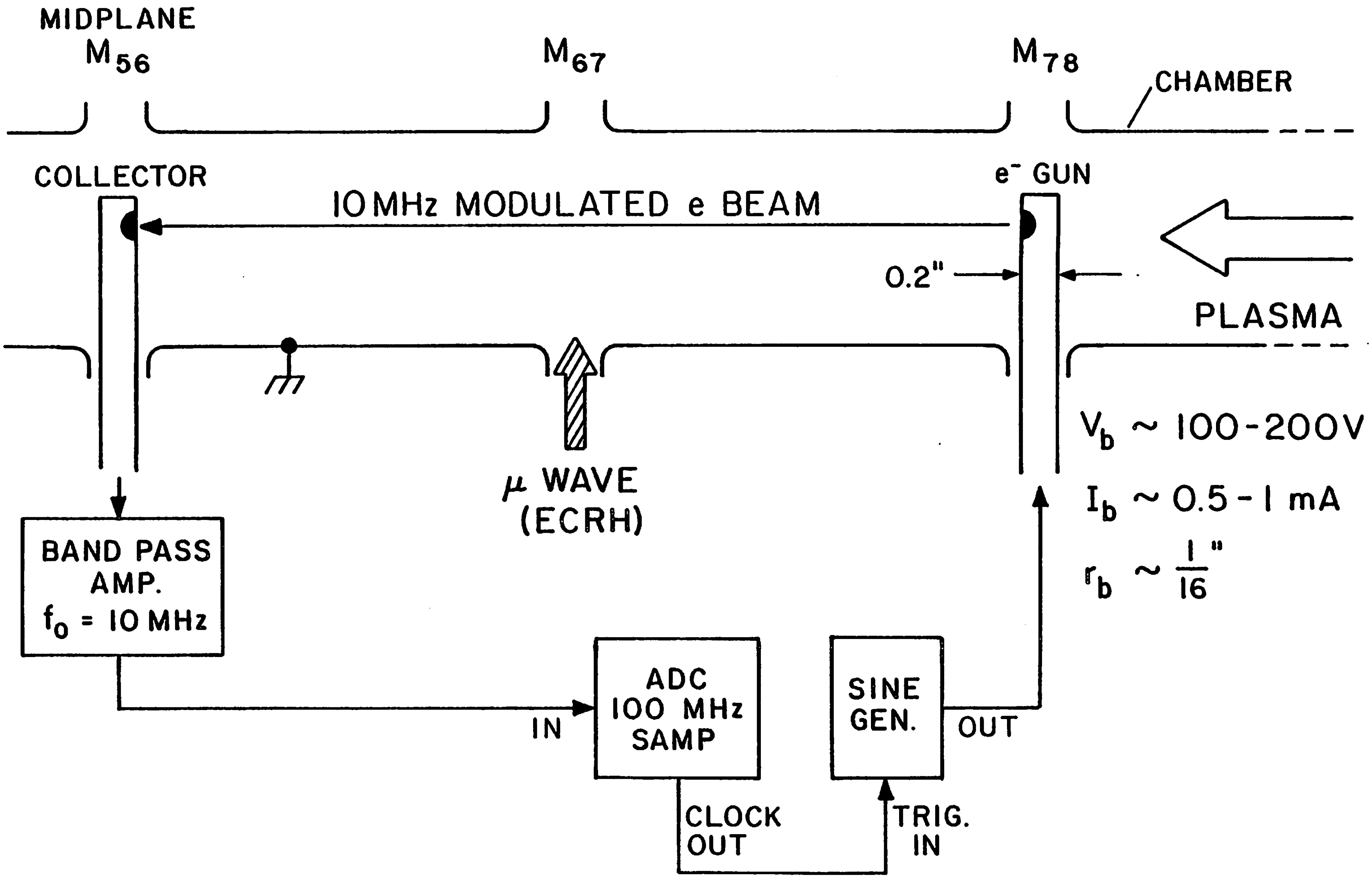
MIDPLANE
M_{56}
M_{67}
M_{78}
CHAMBER
COLLECTOR
e^- GUN
10 MHz MODULATED e BEAM
0.2"
PLASMA
μ WAVE
(ECRH)
$V_b \sim 100\text{-}200V$
$I_b \sim 0.5 - 1$ mA
$r_b \sim \frac{1}{16}$"
BAND PASS
AMP.
$f_0 = 10$ MHz
IN
ADC
100 MHz
SAMP
SINE
GEN.
OUT
CLOCK
OUT
TRIG.
IN

Fig. 2

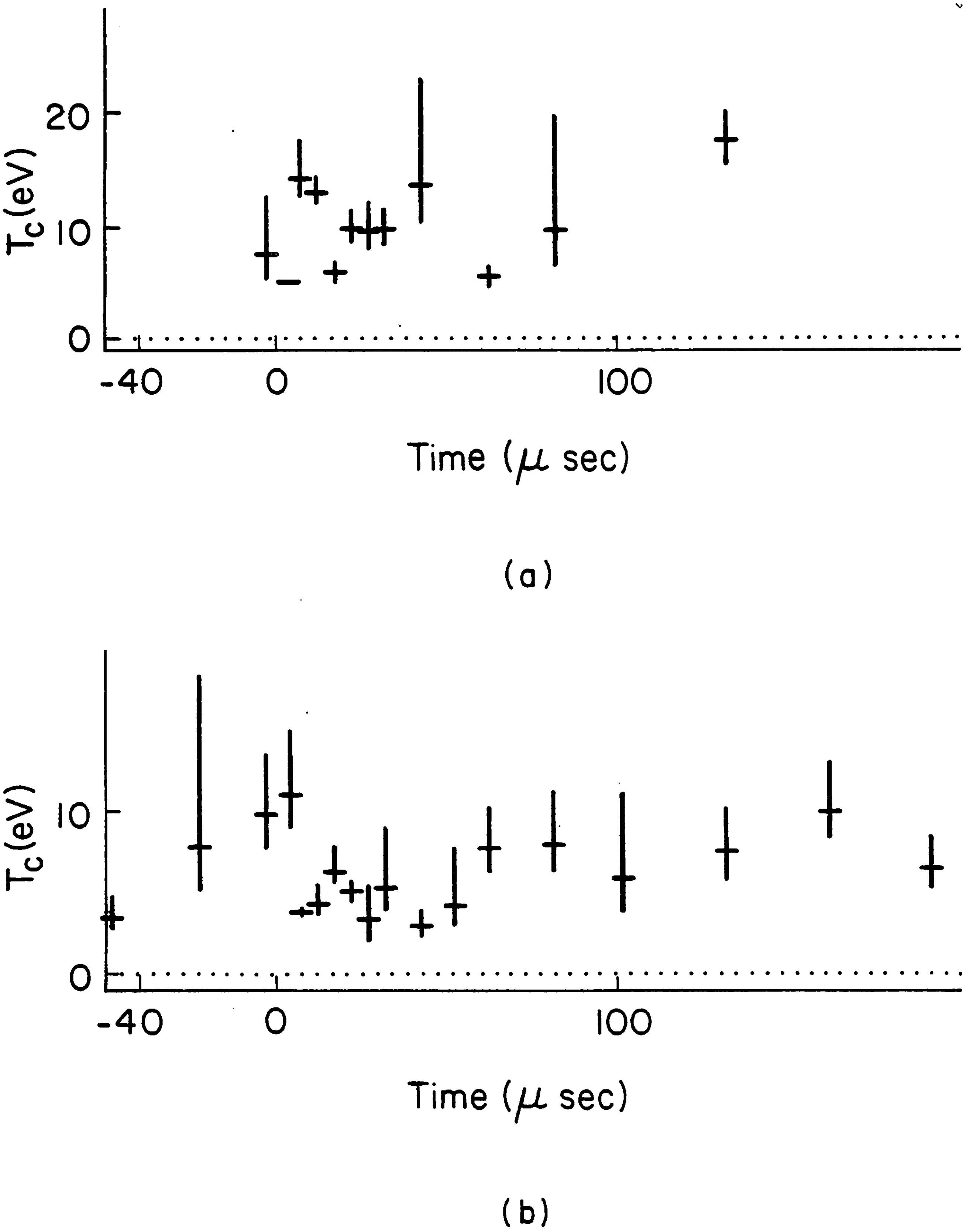

Fig. 3

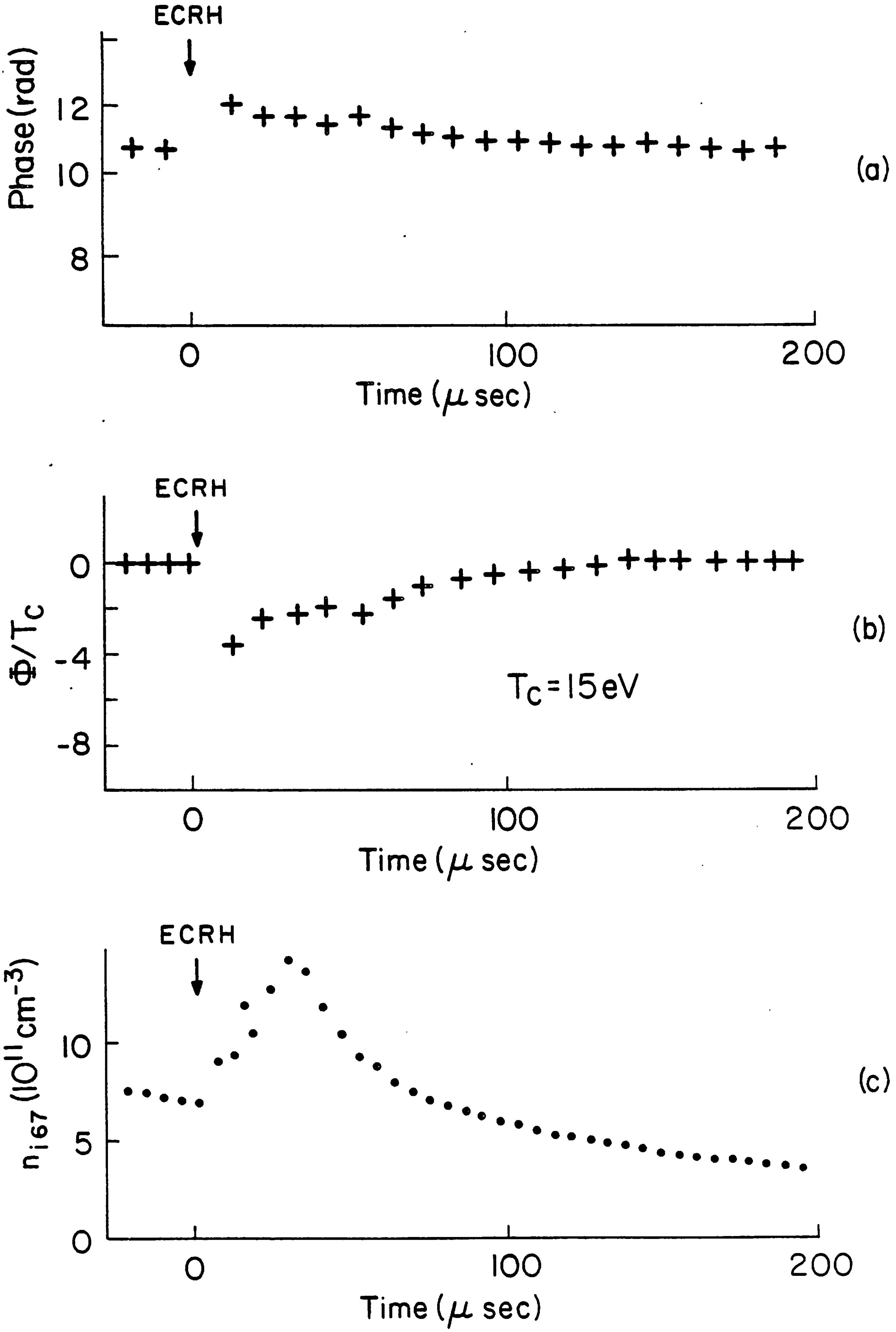
ECRH
Phase (rad)
12
10
8
0
100
200
Time (μ sec)
(a)
ECRH
Φ/Tc
0
-4
-8
Tc = 15 eV
0
100
200
Time (μ sec)
(b)
ECRH
n_i67 (10^11 cm^-3)
10
5
0
0
100
200
Time (μ sec)
(c)

Fig. 4

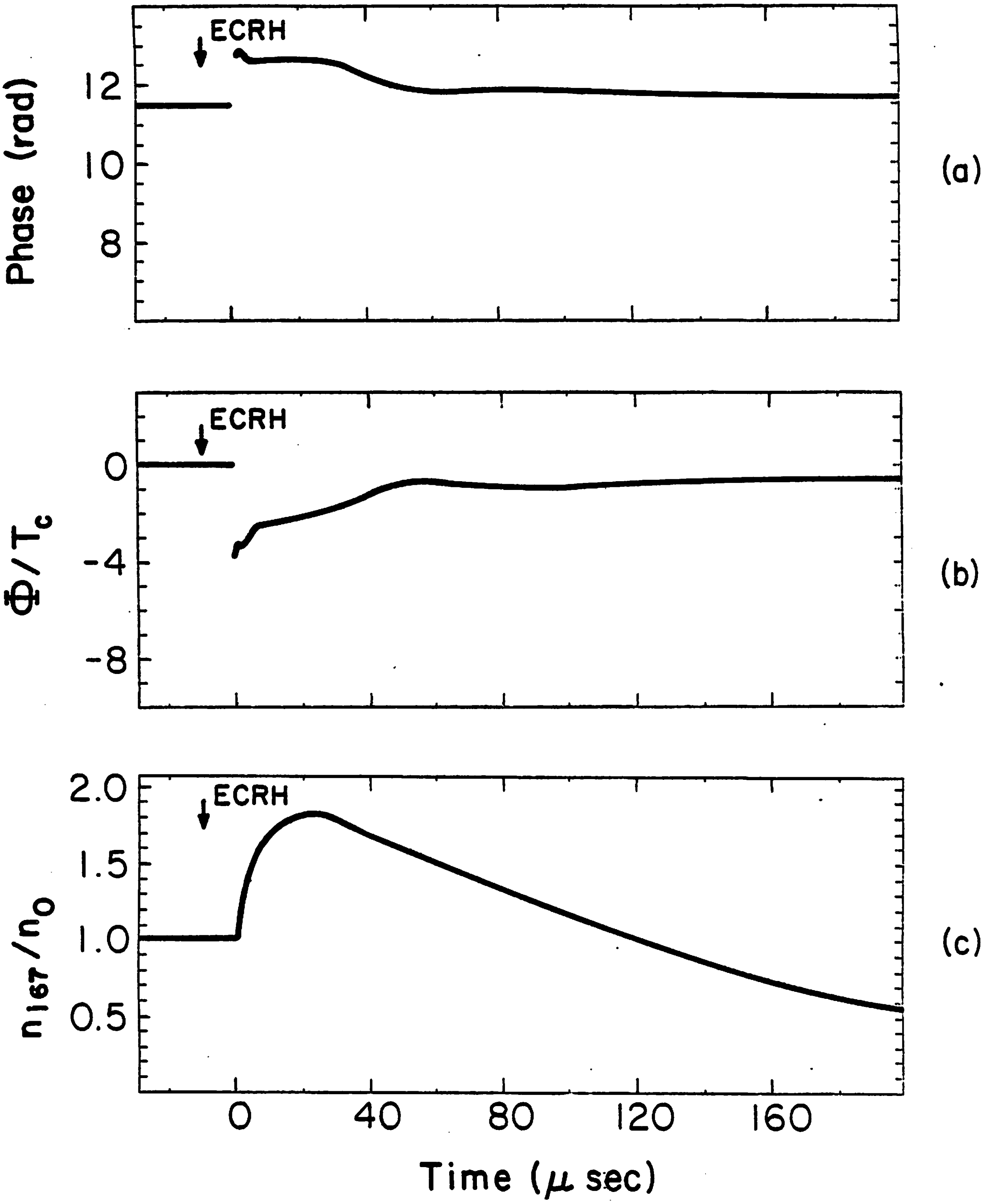
ECRH
Phase (rad)
12
10
8
(a)
ECRH
Φ/T_c
0
-4
-8
(b)
ECRH
n_{167}/n_0
2.0
1.5
1.0
0.5
(c)
0
40
80
120
160
Time (μ sec)

Fig. 5

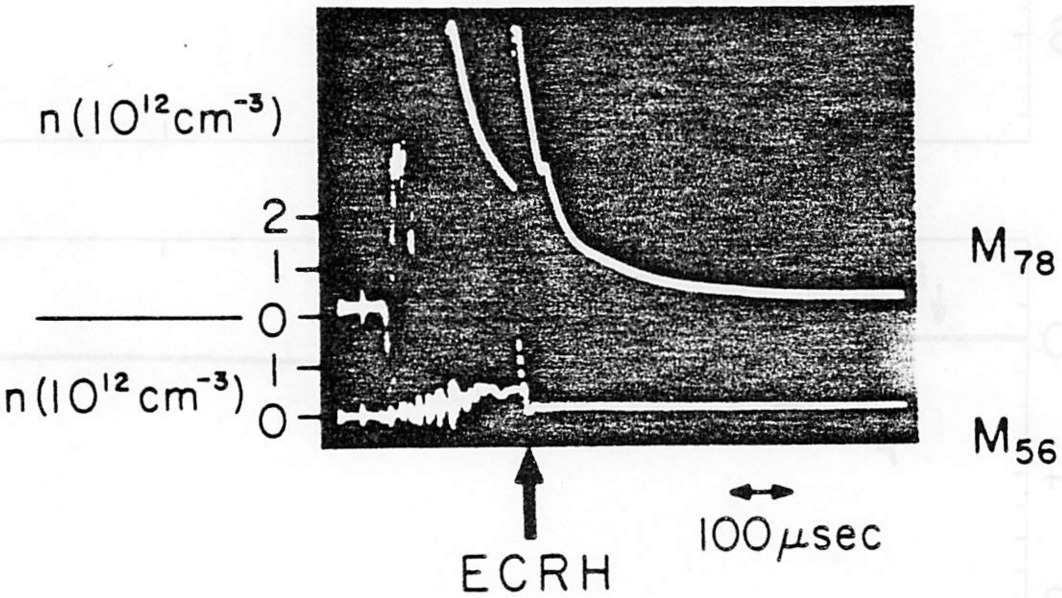

Fig. 6

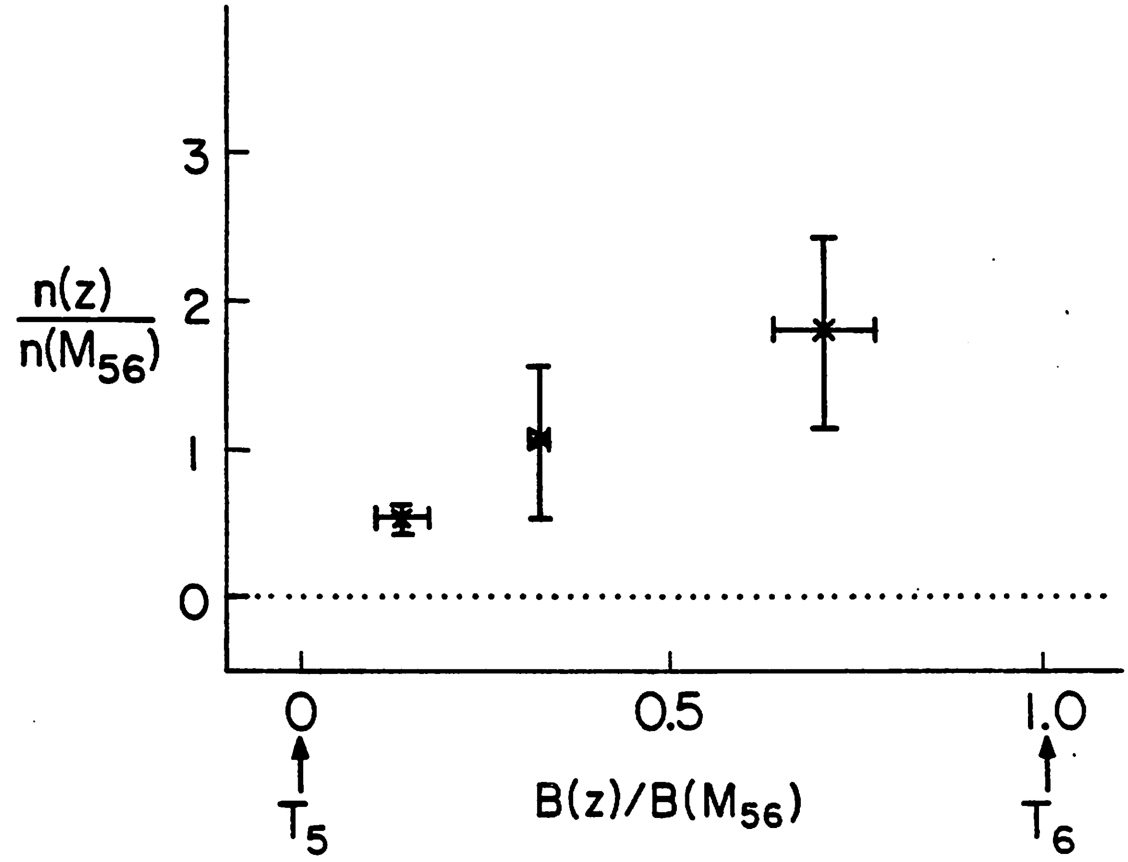

Fig. 7

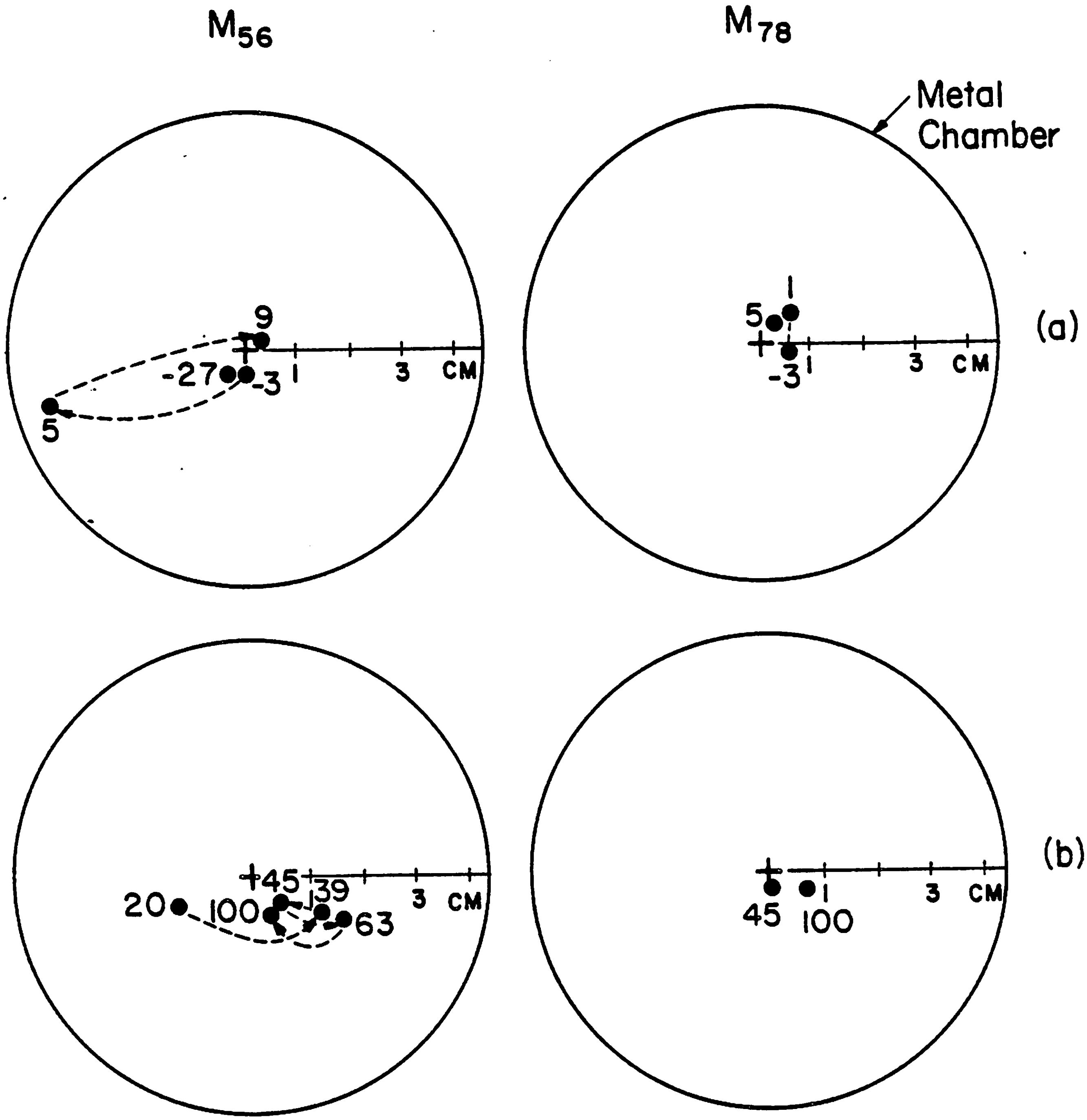
M56
M78
Metal Chamber
9
-27
-3
1
3
CM
5
1
5
-3
1
3
CM
(a)
+45
20
100
139
63
3
CM
45
100
1
3
CM
(b)

Fig. 8

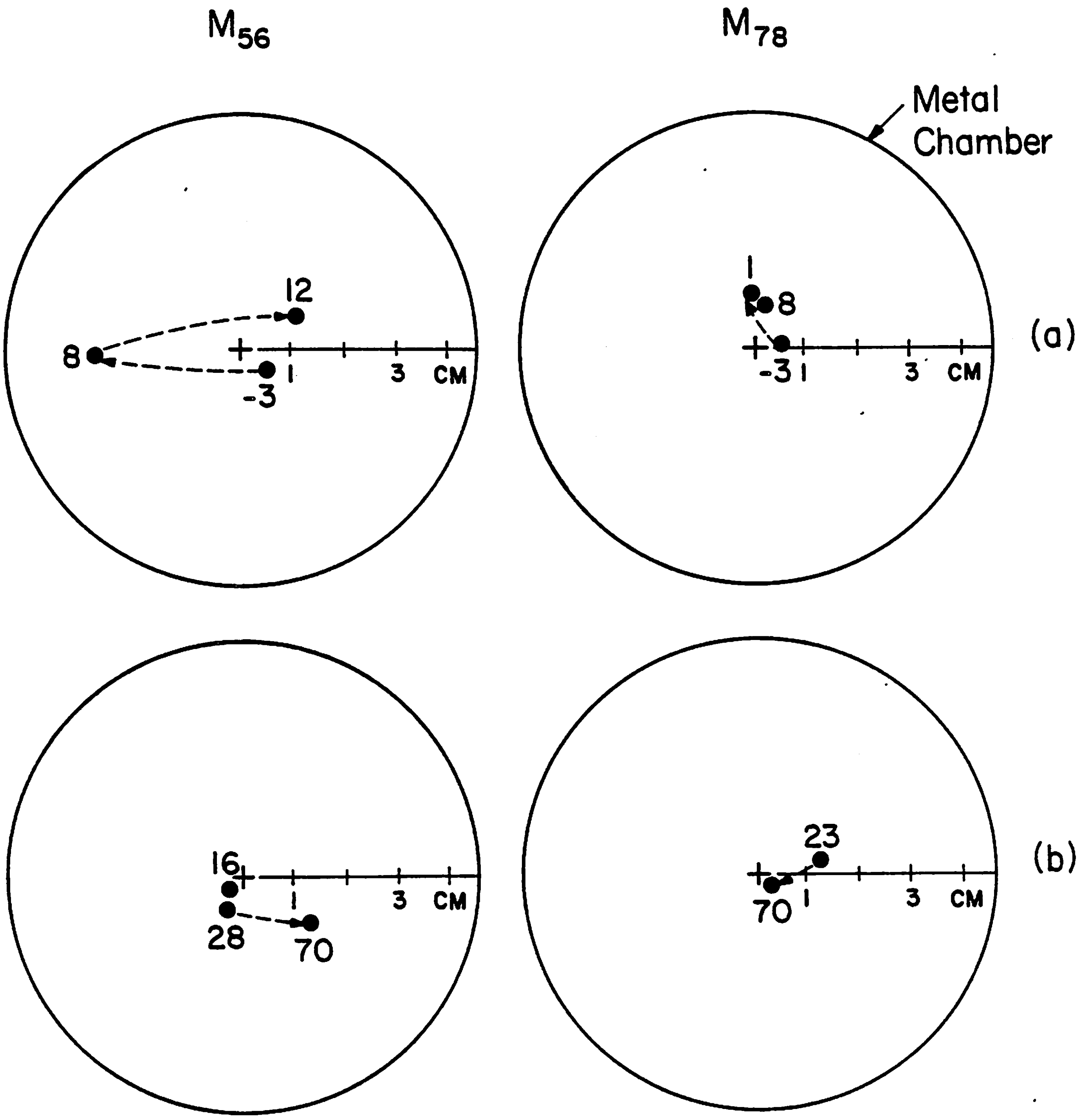
M56
M78
Metal Chamber
12
8
-3
1
3
CM
1
8
-3
1
3
CM
(a)
16
28
70
1
3
CM
23
70
1
3
CM
(b)

Fig. 9

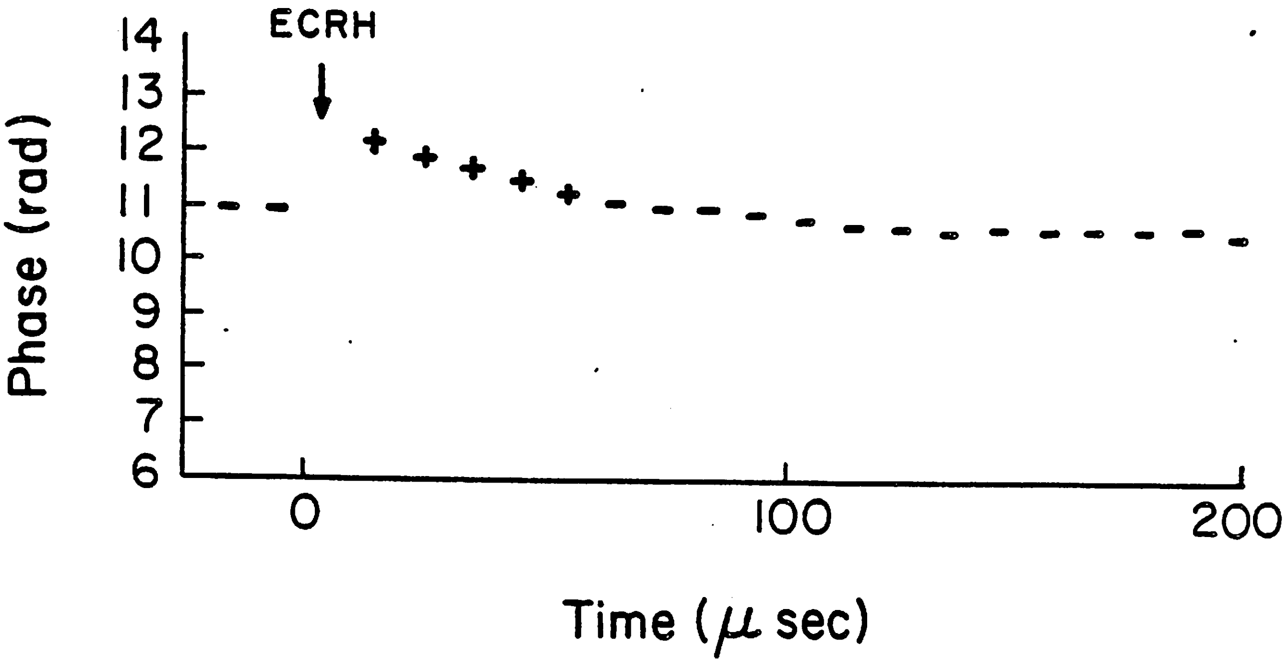

Fig. 10

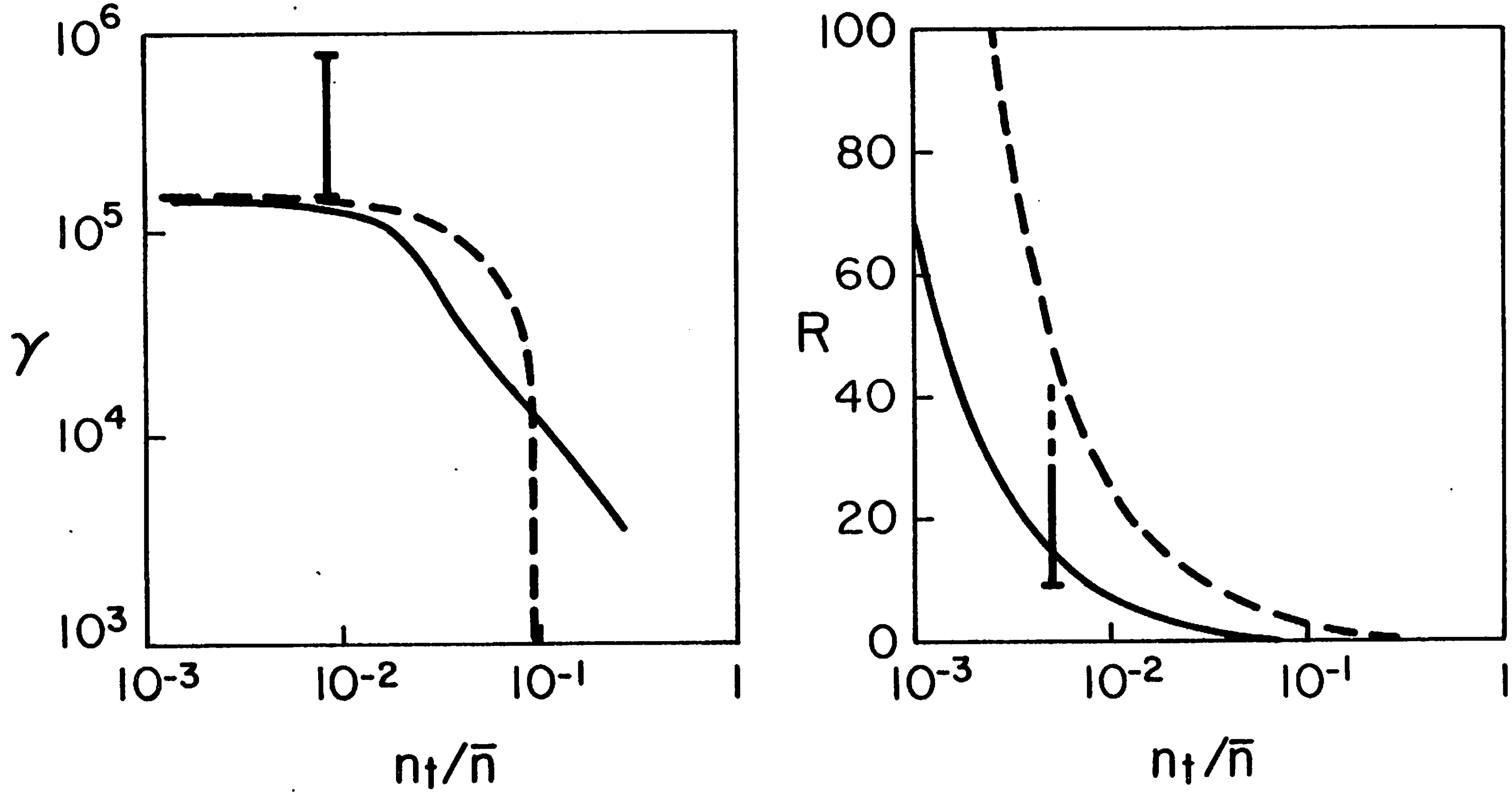
10^6
10^5
10^4
10^3
γ
10^{-3}
10^{-2}
10^{-1}
1
$n_t/\bar{n}$
100
80
60
40
20
0
R
10^{-3}
10^{-2}
10^{-1}
1
$n_t/\bar{n}$

(a)

(b)

Fig. 11